THE ASTROPHYSICAL JOURNAL, 675:303–315, 2008 March 1
© 2008. The American Astronomical Society. All rights reserved. Printed in U.S.A.

HIGH-EXCITATION OH AND H_2O LINES IN MARKARIAN 231: THE MOLECULAR SIGNATURES OF COMPACT FAR-INFRARED CONTINUUM SOURCES[1]

EDUARDO GONZÁLEZ-ALFONSO
Universidad de Alcalá de Henares, Departamento de Física, Campus Universitario,
E-28871 Alcalá de Henares, Madrid, Spain; eduardo.gonzalez@uah.es

HOWARD A. SMITH AND MATTHEW L. N. ASHBY
Harvard-Smithsonian Center for Astrophysics, 60 Garden Street, Cambridge, MA 02138;
hsmith@cfa.harvard.edu, mashby@cfa.harvard.edu

JACQUELINE FISCHER
Naval Research Laboratory, Remote Sensing Division, Washington, DC 20375; jackie.fischer@nrl.navy.mil

LUIGI SPINOGLIO
Istituto di Fisica dello Spazio Interplanetario, CNR via Fosso del Cavaliere 100, I-00133 Roma, Italy;
luigi.spinoglio@ifsi-roma.inaf.it

AND

TIMOTHY W. GRUNDY
Space Science and Technology Department, Rutherford Appleton Laboratory, Chilton, Didcot, Oxfordshire, OX11 0QX, UK;
t.w.grundy@rl.ac.uk
Received 2007 August 18; accepted 2007 November 18

ABSTRACT

The *ISO* LWS far-infrared spectrum of the ultraluminous galaxy Mrk 231 shows OH and H_2O lines in absorption from energy levels up to 300 K above the ground state, and emission in the [O I] 63 μm and [C II] 158 μm lines. Our analysis shows that OH and H_2O are radiatively pumped by the far-infrared continuum emission of the galaxy. The absorptions in the high-excitation lines require high far-infrared radiation densities, allowing us to constrain the properties of the underlying continuum source. The bulk of the far-infrared continuum arises from a warm ($T_{\rm dust} = 70$–100 K), optically thick ($\tau_{100\mu{\rm m}} = 1$–2) medium of effective diameter 200–400 pc. In our best-fit model of total luminosity $L_{\rm IR}$, the observed OH and H_2O high-lying lines arise from a luminous ($L/L_{\rm IR} \sim 0.56$) region with radius $\sim$100 pc. The high surface brightness of this component suggests that its infrared emission is dominated by the AGN. The derived column densities $N({\rm OH}) \gtrsim 10^{17}$ cm^{-2} and $N({\rm H_2O}) \gtrsim 6 \times 10^{16}$ cm^{-2} may indicate X-ray dominated region (XDR) chemistry, although significant starburst chemistry cannot be ruled out. The lower-lying OH, [C II] 158 μm, and [O I] 63 μm lines arise from a more extended ($\sim$350 pc) starburst region. We show that the [C II] deficit in Mrk 231 is compatible with a high average abundance of C^+ because of an extreme overall luminosity to gas mass ratio. Therefore, a [C II] deficit may indicate a significant contribution to the luminosity by an AGN, and/or by extremely efficient star formation.

Subject headings: galaxies: abundances — galaxies: individual (Mrk 231) — galaxies: ISM — galaxies: starburst — infrared: galaxies — radiative transfer

1. INTRODUCTION

The peculiar ultraluminous infrared galaxy (ULIRG; $L_{\rm IR} \geq 10^{12}$ $L_\odot$) Markarian 231 (Mrk 231, 12540+5708) is the most luminous infrared galaxy in the local universe, with a 8–1000 μm luminosity of 3.2×10^{12} $L_\odot$ (Sanders et al. 2003), and may be a representative example of the link between active galactic nuclei (AGNs) and nuclear starbursts (Scoville 2004). A QSO-like nucleus is evident from many observations: optically it is classified as a Type 1 Seyfert (Boksenberg et al. 1977; Cutri et al. 1984; Baan et al. 1998), it exhibits UV through IR polarization and broad absorption lines (Smith et al. 1995), it has compact X-ray emission (e.g., Gallagher et al. 2002) and extremely compact mid-infrared emission (Soifer et al. 2000), and in the radio it is variable and possesses a parsec-scale jet (Ulvestad et al. 1999; Taylor et al. 1999). Nevertheless, there is also evidence of a compact starburst in these results as well as in Very Large Array (VLA) observations of H I 21 cm absorption (Carilli et al. 1998), near-infrared observations (Tacconi et al. 2002), and millimeter CO interferometry (Bryant & Scoville 1996; Downes & Solomon 1998, hereafter DS98). Estimates for the starburst luminosity range from 1/3 to 2/3 of the bolometric luminosity (Davies et al. 2004; DS98).

Molecular observations have provided important clues about the concentration and kinematics of the gas in Mrk 231. DS98 showed the presence of an inner nuclear disk of radius $\sim$460 pc in CO(2–1), and a more extended disk with lower brightness. Most of the molecular gas has been found to be dense ($\sim 10^4$ cm^{-3}) and warm ($\sim$70 K) from recent observations of CO and HCN submillimeter lines (Papadopoulos et al. 2007, hereafter PIW07). Lahuis et al. (2007) have inferred embedded starburst chemistry in Mrk 231 and other ULIRGs based on mid-IR *Spitzer* observations of rovibrational bands of warm/hot HCN and C_2H_2, while Graciá-Carpio et al. (2006) and Aalto et al. (2007) have inferred XDR chemistry and/or radiative pumping based on anomalous intensity ratios of millimeter lines of HCN, HNC, and HCO^+.

---

[1] Based on observations with the *Infrared Space Observatory*, an ESA project with instruments funded by ESA Member States (especially the principal investigator countries: France, Germany, Netherlands, and the United Kingdom) and with the participation of ISAS and NASA.

The bulk of the luminosity in ULIRGs is emitted at far-infrared (FIR) wavelengths, where a number of molecular tracers are detected, mostly in absorption. Prominent lines of OH and H_2O were detected using *Infrared Space Observatory* (*ISO*) LWS in the FIR spectrum of Arp 220, along with absorption features by radicals such as NH and CH, revealing a chemistry that may be indicative of photodissociation regions (PDRs) with plausible contribution by shocks and hot cores (González-Alfonso et al. 2004, hereafter Paper I). However, those species are also expected to be enhanced in XDRs (Meijerink & Spaans 2005), so that the dominant chemistry in the nuclear regions of ULIRGs remains uncertain. In Paper I, the *ISO*/LWS FIR spectrum of Arp 220 was analyzed by means of radiative transfer calculations, which included a nonlocal treatment of the molecular excitation by absorption of FIR photons. Paper I showed that the population of high-excitation OH and H_2O rotational levels, in evidence from absorption in high-lying lines, is pumped through absorption of FIR continuum photons, a process that requires high FIR radiation densities. The detection of these lines thus not only reveals the chemical and excitation conditions in the absorbing regions, it also sheds light on the size and characteristics of the underlying continuum FIR source in spite of the low angular resolution currently available at these wavelengths.

In this paper we extend our approach of Paper I to the *ISO*/LWS FIR spectrum of Mrk 231, and show that this galaxy spectrum presents striking similarities to that of Arp 220. Specifically, strong absorption in the high-excitation OH and H_2O lines is also seen in Mrk 231. Rotationally excited OH in Mrk 231 has been previously detected via the ${}^2\Pi_{1/2}$ Λ-doublet transitions (Henkel et al. 1987). Very long baseline interferometry (VLBI) observations of the megamaser OH emission at 18 cm wavelength trace an inner torus or disk of size ~100 pc around the AGN (Klöckner et al. 2003), and MERLIN observations were able to map essentially the whole single-dish megamaser OH emission with angular resolution of ≈0.3″ (Richards et al. 2005). We analyze here both the FIR continuum emission and the high-excitation OH and H_2O lines, as well as the [C II] 158 μm and [O I] 63 μm emission lines. In § 2 we present the *ISO* spectroscopic observations of Mrk 231. In § 3 we first analyze simple models for the FIR continuum emission from Mrk 231, and then examine how well those models reproduce the observed FIR emission and absorption lines. Section 4 summarizes our results. We adopt a distance to Mrk 231 of 170 Mpc ($H_0 = 75$ km s^{-1} Mpc^{-1} and $z \approx 0.042$).

2. OBSERVATIONS AND RESULTS

The full 43–197 μm spectrum of Mrk 231 (first shown and discussed by Harvey et al. 1999), was obtained with the LWS spectrometer (Clegg et al. 1996) on board *ISO* (Kessler et al. 1996). In Figure 1, it is compared with that of Arp 220 (Paper I) rescaled to the same distance (170 Mpc). The grating spectral resolution is ~0.3 μm in the 43–93 μm interval (detectors SW1–SW5), and ~0.6 μm in the 80–197 μm interval (detectors LW1–LW5), corresponding to $\Delta v \gtrsim 10^3$ km s^{-1}. The lines are thus unresolved in velocity space. The ≈80″ beam size ensures that all the FIR continuum and line emission/absorption from Mrk 231 (CO size ~4″; DS98) lies within the *ISO* LWS aperture.

The data (TDT numbers 5100540, 18001306, and 60300241) were taken from the highly processed data product (HPDP) data set (called uniformly processed LWS01 data), and reduced using version 10.1 of the Off Line Processing (OLP) Pipeline system (Swinyard et al. 1996). We performed subsequent data processing, including co-addition, scaling, and baseline removing, using the *ISO* Spectral Analysis Package (ISAP; Sturm et al. 1998) and our own routines. In order to obtain a smooth spectrum throughout the whole LWS range, the flux densities given by each detector were corrected by multiplicative scale factors. Corrections were less than 25% except for detectors LW2 and LW3 (100–145 μm), for which the corrections were 30%. We thus attribute an uncertainty of 30% to the overall continuum level, as well as for the line fluxes.

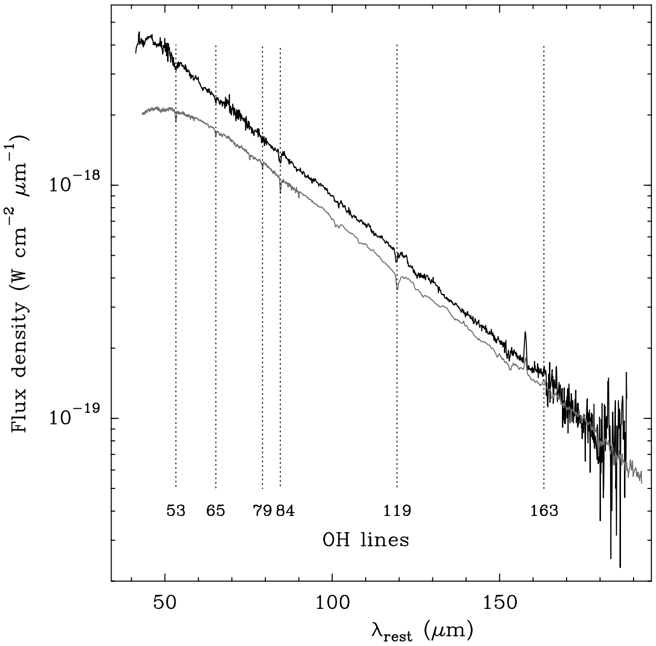

FIG. 1.—Comparison between the FIR emission from Mrk 231 (*black line*) and Arp 220 (*gray line*). The spectrum of Arp 220 has been rescaled to the distance of Mrk 231 (170 Mpc). The position of the OH lines discussed in the text are indicated and labeled with their wavelengths.

Figure 1 shows that the FIR spectra of Mrk 231 and Arp 220 are similar in key aspects (see also Fischer et al. 1999), in particular the prominent molecular absorptions mostly due to OH doublets (that will be referred to hereafter as lines) and the lack of strong fine-structure line emission typically seen in less luminous galaxies. A closer inspection of the pattern of line emission/absorption in both sources is shown in Figure 2, where the continuum-normalized spectra are compared. Of particular interest are the clear detections in both sources of the high-excitation OH $\Pi_{3/2}7/2–5/2$ 84 μm and $\Pi_{3/2}9/2–7/2$ 65 μm lines, with lower level energies of 120 and 290 K, respectively (see § 3). The $3_{30} \rightarrow 2_{21}$ and $3_{31} \rightarrow 2_{20}$ H_2O 66–67 μm lines, both with lower levels at 195 K, are also detected in Mrk 231, as well as the tentatively identified $2_{20} \rightarrow 1_{11}$ line at 101 μm. It is likely that the increased noise level at $\lambda \gtrsim 160$ μm is responsible for the nondetection of the high-excitation $\Pi_{1/2}3/2–1/2$ OH line in Mrk 231, which is seen in strong emission in Arp 220. While the high-excitation OH and H_2O lines at 65–67 μm are of similar strength in Mrk 231 and Arp 220, the H_2O lines at longer wavelengths are undoubtedly weaker in Mrk 231, as seen for the $3_{22} \rightarrow 2_{11}$, $2_{20} \rightarrow 1_{11}$, and $2_{21} \rightarrow 1_{10}$ H_2O lines at 90, 102, and 108 μm, respectively. The weakness of the latter lines in Mrk 231 suggests that the region where the high-lying H_2O lines are formed is relatively weak in the FIR continuum at $\lambda = 90–108$ μm. The Mrk 231 spectrum thus suggests that a warm component with relatively weak contribution to the FIR continuum at $\lambda \gtrsim 80$ μm is responsible for the observed high-excitation absorptions (§ 3.3). Table 1 lists the line fluxes, continuum flux densities at the corresponding wavelengths, and equivalent widths for the lines detected in Mrk 231.

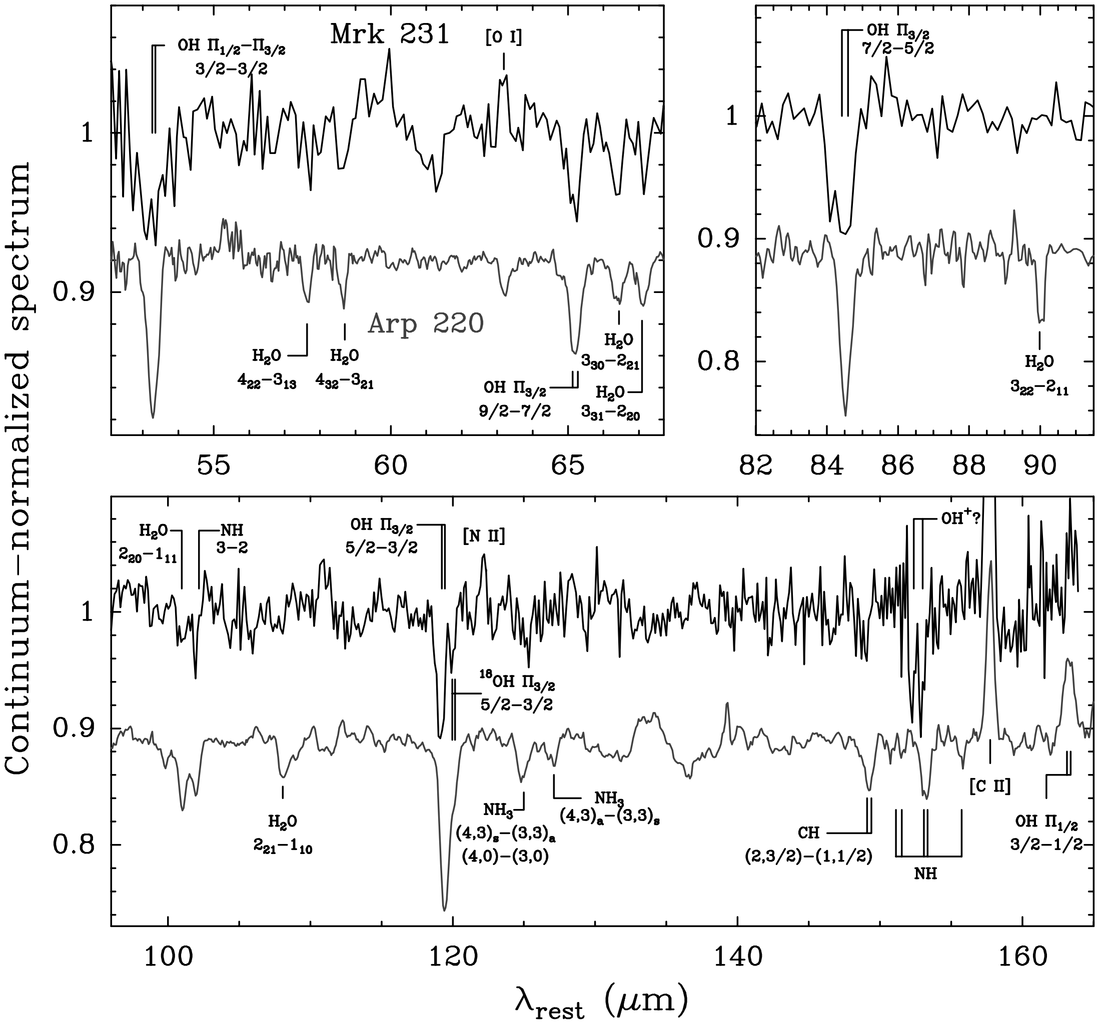

FIG. 2.—Comparison between the continuum-normalized spectra of Mrk 231 (*upper spectra, black lines*) and Arp 220 (*lower spectra, gray lines*). The positions of lines discussed in the text are indicated and labeled.

In the case of Arp 220, we used high spatial resolution continuum measurements available in the literature to infer that Arp 220 is optically thick even in the submillimeter continuum (Paper I; see also Downes & Eckart 2007). The steeper decrease of the flux density with increasing wavelength in Mrk 231, however, suggests that it has lower FIR continuum opacities (Fig. 1). This expectation is further reinforced by the detection in Mrk 231 of the [N II] 122 μm line, a feature not seen in Arp 220 (Fig. 2). Other notable differences between both sources are that the [O I] 63 μm line is observed in emission in Mrk 231 but in absorption in Arp 220, and that the ground-state 119, 53, and 79 μm OH lines are significantly weaker in Mrk 231 (Fig. 2). In modeling Arp 220, we were forced to invoke an absorbing "halo" to account for these lines; in Mrk 231, no such halo is required (§ 3).

In the spectrum of Mrk 231, the main 119.3 μm OH line appears to be slightly blueshifted relative to the expected position, an effect we attribute to the proximity of the line to the edge of the LW3 detector. There is a nearby weaker redshifted feature at 120 μm which coincides with the expected position of the ground $\Pi_{3/2}5/2$–$3/2$ ^{18}OH line, and appears as a marginal feature in both the "up" and "down" grating scans. However, the limited signal-to-noise ratio [$(1.0 \pm 0.4) \times 10^{-20}$ W cm^{-2}], the narrow appearance of the feature ($\approx$0.42 μm), and the fact that it is not blueshifted as the main line, make that assignment only tentative. In Arp 220, the main OH line is not shifted because it does not fall so close to the edge of the detector, as a consequence of the lower redshift of the source. In Arp 220, a redshifted shoulder appears at 120 μm, suggesting the possibility that ^{18}OH may be responsible for it (Paper I). We cannot however be certain that ^{18}OH is detected in any of these sources, but given the high ^{16}OH column densities we derive in some of our models below (§ 3.3) and the fact that values of the ^{16}OH/^{18}OH ratios below the canonical value of 500 may be expected in regions where the interstellar matter (ISM) is highly processed by starbursts (Paper I), our tentative identification should be followed up with future *Herschel Space Observatory* observations with higher spectral resolution and sensitivity. Finally, the spectrum of Mrk 231 shows a broad feature at the position of the $\Pi_{1/2}$–$\Pi_{3/2}3/2$–$3/2$ OH line (53 μm). We note that the blueshifted side of this absorption is coincident with the OH $\Pi_{3/2}11/2$–$9/2$ line, with a lower level energy of 511 K; however, the proximity of this spectral feature to the edge of the SW2 detector precludes any definitive assignment.

The FIR detections of both NH and NH_3 in Arp 220 were reported in Paper I. NH_3 was also detected via the 25 GHz inversion transitions by Takano et al. (2005), who derived a NH_3 column density 6 times higher than our value. The difference likely arises because of the high FIR continuum opacities in Arp 220, which cause the observed FIR absorptions to trace only a fraction of the total gas column. Since there are no such extinction effects

TABLE 1

LINE FLUXES, CONTINUUM FLUX DENSITIES, AND EQUIVALENT WIDTHS FOR THE LINES DETECTED IN THE *ISO* LWS SPECTRUM OF Mrk 231

Species	Transition	$\lambda_{\rm rest}$[a] (μm)	Line Flux[b] (10^{-20} W cm^{-2})	Continuum[c] (10^{-19} W cm^{-2} μm^{-1})	W[d] (10^{-2} μm)
OH	$\Pi_{1/2}$–$\Pi_{3/2}$ 3/2–3/2	53.3	−7.0 ± 2.0	33.5	2.1 ± 0.6
[O I]	$^3P_1$–$^3P_2$	63.2	2.6 ± 0.8	25.0	−1.0 ± 0.3
OH	$\Pi_{3/2}$ 9/2–7/2	65.2	−4.1 ± 0.6	23.8	1.7 ± 0.3
H_2O	3_{30}–2_{21}	66.4	−3.3 ± 0.9	23.1	1.4 ± 0.4
H_2O	3_{31}–2_{20}	67.1	−2.2 ± 0.9	22.7	1.0 ± 0.4
OH	$\Pi_{3/2}$ 7/2–5/2	84.5	−8.6 ± 0.7	13.8	6.2 ± 0.5
H_2O	2_{20}–1_{11}	101	−1.3 ± 0.3	8.70	1.5 ± 0.4
OH	$\Pi_{3/2}$ 5/2–3/2	119.3	−3.6 ± 0.3	5.22	6.9 ± 0.6
[N II]	$^3P_2$–$^3P_1$	121.8	1.5 ± 0.2	4.72	−3.2 ± 0.4
[C II]	$^2P_{3/2}$–$^2P_{1/2}$	157.7	3.7 ± 0.1	1.73	−21.4 ± 0.6

[a] For OH doublets, an average for the two components is given.

[b] Errors do not include calibration uncertainties in the continuum level. Negative (positive) values indicate that the line is detected in absorption (emission).

[c] Uncertainties in the continuum level are less than 30%.

[d] Equivalent widths are positive (negative) for lines observed in absorption (emission).

at 25 GHz, the NH_3 inversion transitions are expected to trace higher NH_3 column densities. Figure 2 shows that, by contrast, the NH_3 lines are not detected in Mrk 231, although the relatively high noise at 125 μm does not rule out future detection of NH_3 with *Herschel* at a level similar to that of Arp 220.

There are two marginally detected (2.5 σ level) spectral features seen at 153.0 and 152.3 μm in the Mrk 231 spectrum (Fig. 3). Although close to the expected position of the main NH feature at 153.22 μm, the 153.0 μm feature appears significantly shifted by 0.25 μm from it, and better coincides with the position of the $OH^+ 2_3$–1_2 line. Also, the 152.3 μm feature lies at 0.1 μm from the expected position of the $OH^+ 2_2$–1_1 line. In Paper I, we also suggested that OH^+ could contribute to the spectrum of Arp 220 for two reasons: (1) our models were unable to reproduce, using NH and NH_3, the observed strong absorption at 102 μm, which coincides with the expected position of the $OH^+ 3_4$–2_3 line; (2) there was an absorption feature at 76.4 μm that, if real, could be attributed to the $OH^+ 4_4$–3_3 transition. Since OH^+ has never been detected in the Galactic interstellar medium or that of any galaxy, here we only highlight the intriguing possibility of its detection in two ULIRGs. Sensitive, higher-resolution *Herschel* observations are needed to resolve this tantalizing speculation.

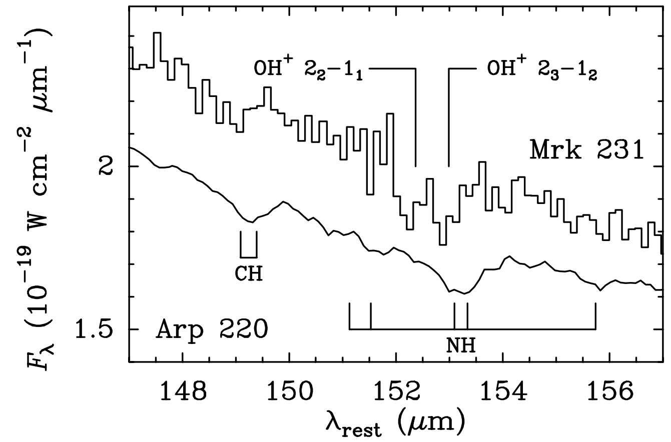

FIG. 3.—Comparison between the spectra of Mrk 231 (*upper spectrum, histogram*) and Arp 220 (*lower spectrum, solid line*) around 152 μm. The spectrum of Arp 220 has been rescaled to the distance of Mrk 231 (170 Mpc). The position of the NH, CH, and OH^+ lines are indicated and labeled.

The luminosity of the [C II] $^2P_{3/2}$–$^2P_{1/2}$ fine-structure line at 158 μm is 2.5 times stronger in Mrk 231 than in Arp 220, but given the higher FIR luminosity of this source (Fig. 1), the [C II] to FIR luminosity ratios are rather similar, with values of 2.5×10^{-4} and 2.1×10^{-4} for Mrk 231 and Arp 220, respectively (Luhman et al. 2003). These are among the lowest values found in galaxies, illustrating the so-called [C II] deficit found in ULIRGs. The [C II] line emission from Mrk 231 is analyzed in § 3.4.

3. ANALYSIS

3.1. *Models for the FIR Continuum*

Figure 4 illustrates several ways that the FIR to millimeter continuum can be fit and interpreted. We first modeled (model A in Fig. 4*a*) the FIR source in Mrk 231 as an ensemble of identical dust clouds, each of which is heated by its own single central luminosity source. The representative cloud is assumed to be spherical, with radius R_c, and is divided into concentric shells whose dust temperatures are computed from the balance of heating and cooling (González-Alfonso & Cernicharo 1999). We used a mixture of silicate and amorphous carbon grains with optical constants from Preibisch et al. (1993) and Draine (1985). The stellar continuum was taken from Leitherer et al. (1999), but results depend only weakly on this choice because the intrinsic continuum is absorbed by the dust and re-emitted at infrared wavelengths. Once the equilibrium temperatures are obtained for each shell, the resulting continuum emission from the cloud is computed and multiplied by N_c, the number of clouds in the source required to match the absolute flux densities. This scaled spectrum is shown in Figure 4*a*. The other three models (B, C, and D, shown in Figs. 4*b*–4*d*) use graybodies with uniform dust temperatures T_d to characterize the continuum emission (e.g., Roche & Chandler 1993; Armus et al. 2007).

Assuming that the individual clouds do not overlap along the line of sight, our results do not depend particularly on the radius or luminosity adopted for the model individual cloud because identical results are obtained if R_c is multiplied by a factor of α, the luminosity by α^2, N_c by α^{-2}, and the continuum opacity is kept constant (see Paper I). The models are thus characterized by the luminosity of the whole ensemble, the radial opacity of the clouds at a given wavelength (which we adopt to be 100 μm: $\tau_{100\mu\rm m}$), and the equivalent radius of the source, defined as $R_{\rm eq} = N_c^{1/2} R_c$. These parameters are listed in Table 2.

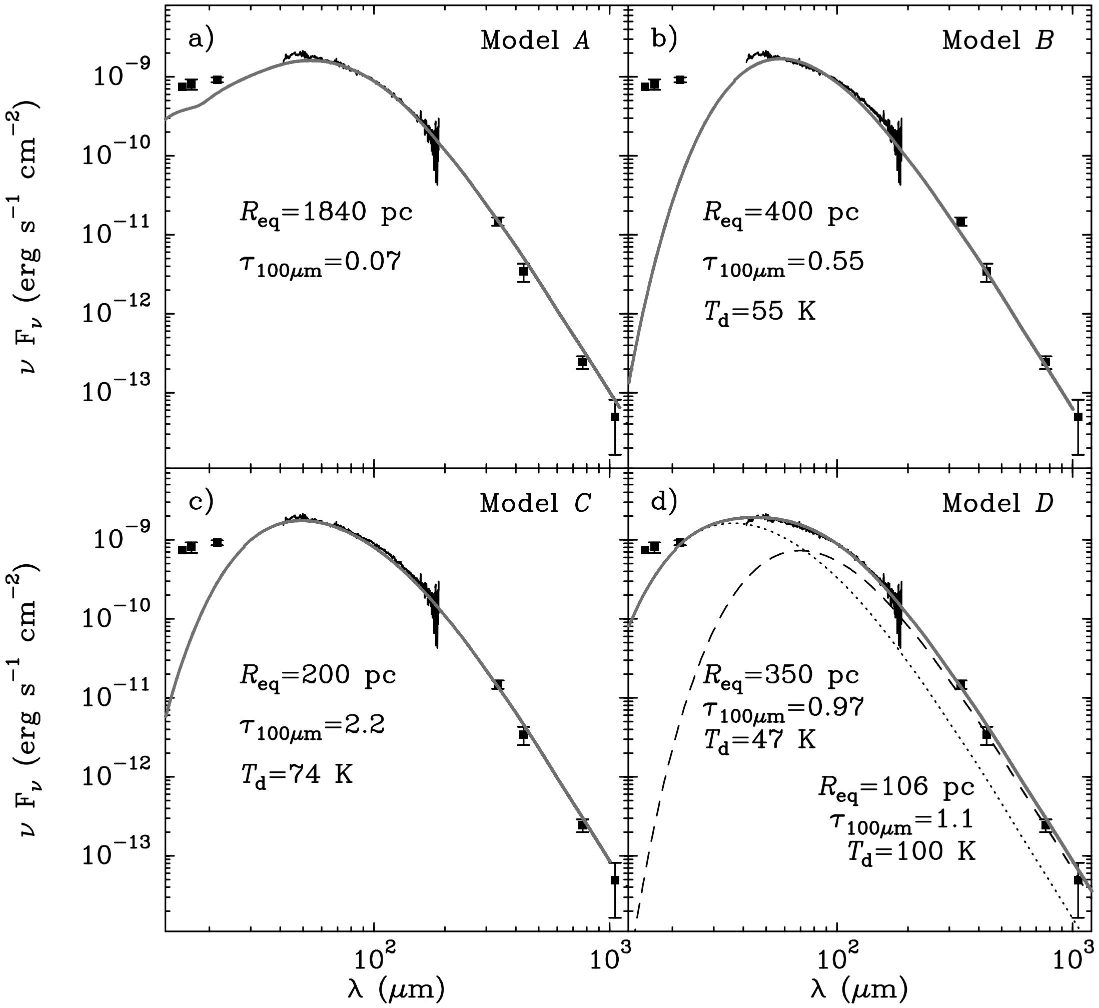

FIG. 4.—Different models for the FIR continuum emission from Mrk 231. The whole set of parameters that characterize models A, B, C, and D are listed in Table 2. Flux densities at 800 and 1100 μm are taken from Roche & Chandler (1993; corrected for nonthermal emission), at 450 μm from Rigopoulou et al. (1996), at 350 μm from Yang & Phillips (2007), and at $\lambda < 25$ μm from Rieke (1976).

In model A, the individual clouds are optically thin so that some degree of cloud overlap would yield a similar fit to the continuum while decreasing the value of $R_{\rm eq}$. For instance, if the clouds are distributed in a spherical volume, $R_{\rm eq} = N_c^{1/3} R_c$, giving $R_{\rm eq} = 400$ pc for clouds with $R_c = 20$ pc. However, the predicted opacity through the modeled region, $N_c^{1/3}\tau_{100\,\mu\rm m}$, will be much higher than that of an individual cloud, and this physical situation is already described in models B–C, where higher opacities along the line of sight and a more compact region of FIR emission are assumed. In order to avoid this model redundancy, we choose our continuum models such that an individual cloud describes the characteristic continuum opacity ($\tau_{100\,\mu\rm m}$ in Table 2) and dust temperature through the whole region (disk), so that the resulting extent of the FIR emission is $R_{\rm eq} = N_c^{1/2} R_c$.

The observed continuum can be reproduced from model A's cloud ensemble that is optically thin in the FIR. Model A also predicts that the starburst dominates the continuum for $\lambda \gtrsim 15$ μm, while the torus/disk around the AGN would then dominate the mid-infrared continuum, in qualitative agreement with the models by Farrah et al. (2003). The equivalent radius of the starburst is slightly larger than the radius of the outer disk observed by DS98. Because $\tau_{100\,\mu\rm m}$ is low and $R_{\rm eq}$ is high, this model predicts that the *FIR radiation density* is low, a prediction that is not consistent with our models of the observed OH line strengths (§ 3.2).

TABLE 2

MODELS FOR THE CONTINUUM EMISSION

Model	Component	$\tau_{100\,\mu\rm m}$	$R_{\rm eq}$ (pc)	$N(H_2)$[a] (cm^{-2})	T_d (K)	$T_{\rm rad}$ (K)	M ($M_\odot$)	L ($L_\odot$)	$L/L_{\rm IR}$
A....................................	...	6.8×10^{-2}	1830	4.6×10^{22}	Variable[b]	23	1.0×10^{10}	2.4×10^{12}	0.72
B....................................	...	0.55	400	3.7×10^{23}	55	44	4.0×10^{9}	1.7×10^{12}	0.50
C....................................	...	2.2	200	1.5×10^{24}	74	71	4.0×10^{9}	2.0×10^{12}	0.61
D....................................	Warm	1.1	106	7.2×10^{23}	100	85	5.5×10^{8}	1.8×10^{12}	0.56
D....................................	Cold	0.97	350	6.5×10^{23}	47	42	5.3×10^{9}	7.4×10^{11}	0.22

[a] A gas-to-dust mass ratio of 100 is assumed, together with a mass-absorption coefficient for dust of 44 cm^2 g^{-1} at 100 μm.

[b] The temperature is calculated from the balance between heating and cooling; see text for details.

As both $\tau_{100\,\mu\rm m}$ and T_d are increased in models B and C, the radiation density increases and, therefore, the equivalent size required to reproduce the observed emission becomes smaller. As a consequence, models B and C predict increasing compactness of the dust clouds responsible for the FIR emission, with $R_{\rm eq} =$ 400 and 200 pc, respectively. With a single-component model, however, $R_{\rm eq}$ cannot be reduced more than in model C without degrading the quality of the fit. However, a two-component model as shown in model D is able to reproduce the FIR emission, invoking a quite compact (~100 pc) and warm (100 K) component ($D_{\rm warm}$), and a colder and more extended one that dominates at $\lambda > 80$ μm ($D_{\rm cold}$).

A convenient way to characterize the radiation density in the modeled regions is to compute the radiation temperature at 100 μm from

$$T_{\rm rad}(100\ \mu{\rm m}) = \frac{h\nu}{k\ln\left[1+\left(2h\nu^3\Omega/c^2F_{100\,\mu\rm m}\right)\right]}, \qquad (1)$$

where $\Omega = \pi N_c R_c^2/D^2$ is the solid angle subtended by the modeled source, $F_{100\,\mu\rm m}$ is the predicted flux density at 100 μm, and other symbols have their usual meanings. $T_{\rm rad}(100\ \mu{\rm m})$ is also listed in Table 2, together with the gas mass, luminosity, and fraction of the bolometric luminosity for each model. The calculated gas masses assume a gas-to-dust mass ratio of 100. In all cases, they are lower than the dynamical masses determined by DS98 when $R_{\rm eq}$ is identified with the radial extent of the source (and therefore compatible with the inferred rotation velocities in the disk). Our inferred masses are consistent in models B–D with the mass inferred by PIW07, but are in all cases higher, by at least a factor of 2, than the gas masses obtained by DS98. This discrepancy may be explained in at least four possible, different ways: (1) the physical radial extent of the cloud ensemble, which accounts for cloud filling, is given by $R_T = f^{-1/2}R_{\rm eq}$, where f is the area filling factor, so that $R_{\rm eq}$ is a lower limit of R_T; (2) our calculated masses depend on the mass-absorption coefficient for dust, which we have assumed to be $\kappa_{1300\,\mu\rm m} = 0.33$ cm^2 g^{-1} based on a mixture of silicate and amorphous carbon grains (Preibisch et al. 1993; Draine 1985), but could be up to a factor ~6 higher if the dust is mainly composed of fluffy aggregates (Kruegel & Siebenmorgen 1994); (3) the gas-to-dust mass ratio may depart significantly from the standard value of 100; and (4) the masses derived by DS98 for Mrk 231 could be lower limits in the light of the submillimeter CO emission reported by PIW07. A combination of these factors may explain our higher values.

The luminosities in Table 2 account for 50%–80% of the observed 8–1000 μm infrared luminosity. Model A implicitly assumes that the calculated luminosity has a starburst origin; the luminosity from model B and from the cold component of model D are also attributable to the starburst in view of the spatial extent of the modeled source. Since model C and the warm component of model D are more compact, a combination of AGN and starburst contributions is more plausible. The surface brightness in model C is 4×10^{12} $L_\odot$ kpc^{-2}, a factor of 2 higher than the peak global value found in starburst galaxies by Meurer et al. (1997), suggesting an important (but uncertain) contribution by the AGN to the observed FIR emission (Soifer et al. 2000). In addition, the luminosity-to-mass ratio of 500 $L_\odot/M_\odot$ coincides with the uppermost limit proposed by Scoville (2004) for a starburst. The very high surface brightness (1.3×10^{13} $L_\odot$ kpc^{-2}) and luminosity-to-mass ratio (~3300 $L_\odot/M_\odot$) of the warm component of model D ($D_{\rm warm}$), as well as its compactness, persuasively indicate that this component is most probably dominated by the AGN. The most plausible relative contributions by the AGN and the starburst to $D_{\rm warm}$ are discussed in § 4.

In summary, different approaches can be used to successfully fit the observed FIR continuum emission, with the properties of the clouds that emit that radiation in these approaches spanning a wide range of possible physical scenarios. But *ISO* LWS has provided us with spectroscopic information, and we show next how the observed high excitation OH and H_2O lines impose important constraints on these continuum models.

3.2. *Equivalent Widths*

We analyze the OH equivalent widths assuming that the OH molecules form a screen in front of the IR source. The strengths of the $\Pi_{3/2}7/2$–$5/2$ and $9/2$–$7/2$ OH doublets at 84 and 65 μm enable us to conclude that the excited OH covers a substantial fraction of the FIR emission region. Assuming that each line of the 84 μm doublet absorbs all the background 84 μm continuum over a velocity range of 250 km s^{-1} *along each line of sight*, and that there is no significant re-emission in the line, the covering factor is ~50%. This value may be considered a lower limit for the following reasons. The submillimeter CO line profiles shown by PIW07 have FWHMs of 200–250 km s^{-1}, and the lines are expected to be broadened by velocity gradients and, in particular, by the disk rotation; therefore, the velocity range of 250 km s^{-1} assumed above is probably an upper limit. DS98 inferred local turbulent velocities of up to 60 km s^{-1} at inner radii (100 pc) and decreasing as $r^{-0.3}$. If we adopt an intrinsic Gaussian line profile with the highest value of the turbulent velocity, $\Delta V = 60$ km s^{-1}, and saturate the 84 μm line to the degree that an effective width[2] of 250 km s^{-1} is obtained for each component of the doublet, the derived 84 μm foreground opacity at line center is ~50, but the high column density required for this opacity is hard to reconcile with that inferred from the other observed OH line strengths (§ 3.3). Finally, some significant re-emission in the 84 μm OH line is expected because the $\Pi_{3/2}9/2$–$7/2$ OH line at 65 μm that originates from its upper level is detected in absorption. We therefore conclude that the observed 84 μm OH absorption is widespread, and probably covers the bulk of the 84 μm continuum emission regions. On the other hand, the opacities in the high-lying 65 μm line should only be moderate; for reference, if we adopt for each component an upper limit of 150 km s^{-1} on the effective velocity interval for the absorption at each sight line, the minimum covering factor for this line is then 25%. It is therefore possible that the OH responsible for the 65 μm absorption does not entirely coincide with that producing the 84 μm absorption but is only a fraction of the latter, consistent with its lower energy level being at nearly 300 K. Nevertheless, for the sake of simplicity, we assume in this section that both lines arise in the same region—one that, on the basis of the 84 μm OH strength, covers the total FIR continuum. The derived OH column densities will be lower limits, and the inferred properties of the continuum source will be associated with at least ~50% of the observed FIR emission.

The equivalent widths W are then given by

$$W = 2\left[1-\frac{B_\nu(T_{\rm ex})\Omega}{F_\lambda}\right]\int(1-\exp\{-\tau_v\})dv, \qquad (2)$$

where $B_\nu(T_{\rm ex})$ is the blackbody emission at the excitation temperature $T_{\rm ex}$ of the line, $\Omega = \pi R_{\rm eq}^2/D^2$ is the solid angle subtended by the source, F_λ is the observed continuum flux density at the

---

[2] The effective width is defined here as $\int(1-\exp\{-\tau_v\})dv$, where $\tau_v = \tau_0\exp\{-(v/\Delta V)^2\}$ and τ_0 is the line opacity at line center.

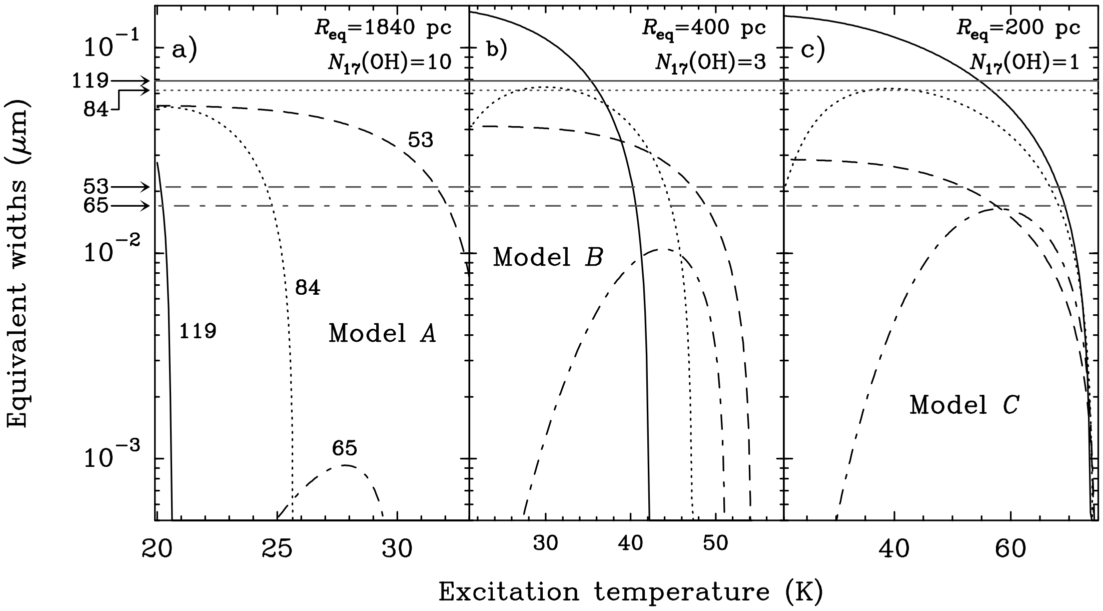

FIG. 5.—Predicted equivalent widths (W) vs. the OH excitation temperature (T_{ex}) for the 119 (*solid curves*), 84 (*dotted curves*), 65 (*dash-dotted curves*), and 53 (*dashed curves*) μm OH doublets. Results are shown for three assumed sizes of the continuum emission, corresponding to the continuum models A, B, and C in Table 2. The observed values are indicated with horizontal lines. N_{17}(OH) is the assumed OH column density in units of 10^{17} cm^{-2}. The equivalent widths are positive if the lines are in absorption; a drop in W with increasing T_{ex} thus indicates that the corresponding line is turning from absorption to emission.

wavelength λ of the line, τ_v is the line opacity at velocity v, and the factor 2 accounts for the two lines that compose a doublet. The values of W are positive for absorption lines, and negative for lines observed in emission. Equation (2) applies both to optically thin and optically thick lines. For optically thin lines, W is proportional to the assumed column density; for very optically thick lines, W becomes insensitive to the column density and scales linearly with the turbulent velocity. Based on DS98, we have adopted $\Delta V = 40$ km s^{-1}, which is probably accurate within 50%.

The fractional level populations and column densities (and hence the opacities), and blackbody temperatures required to obtain W from equation (2) can be estimated from a given column density N(OH), and by assuming that *the excitation temperature* T_{ex} *is the same for all OH transitions*. This assumption is certainly only an approximation. The OH levels are pumped primarily through absorption of FIR photons; this is quite a general model result when both the ground and the excited OH rotational lines (except the 163 μm one) are observed in absorption (see the similar conclusion in Paper I for the case of Arp 220, as well as the case of the H$_2$O lines at 25–45 μm in Orion/IRc2; Wright et al. 2000). When radiative excitation dominates, the level populations tend toward equilibrium with the radiation field within the inner cloud, and the excitation temperatures are similar for all transitions in those regions. However, the observed absorptions are produced close to the cloud boundary where the OH molecules are illuminated from only one side and T_{ex} is less than the radiation temperature. Due to trapping effects, the lines with the highest opacity (119 and 84 μm OH lines) remain more excited than the other lines at inner locations of the region, but their T_{ex} values decrease more steeply outwards and fall below the T_{ex} values of other, thinner lines close to the cloud boundary. The detailed, nonlocal radiative transfer models described in § 3.3 show that the assumption of equal T_{ex} is only approximately valid for the 119 and 84 μm lines, but for the other lines, and in particular for the 65 and 53 μm lines, T_{ex} may be higher or lower depending on position in the region. Nevertheless, the opacities of the 119, 84, 65, and 53 μm lines are mostly determined by the T_{ex} of the 119 and 84 μm lines. As a result, the following analysis of the radiation density (or, equivalently, R_{eq}, required to account for the observed absorptions) is accurate, at least to a first approximation.

The three parameters now required to estimate W from equation (2) are then N(OH), R_{eq}, and T_{ex}. Figure 5 shows the expected values of W for models A, B, and C as a function of T_{ex} for the 119, 84, 65, and 53 μm lines, and compares them with the observed values. Each panel assumes a value of R_{eq} that corresponds to the continuum models A, B, and C described in § 3.1 (see also Table 2). The values of N(OH) used for each model are just reference values discussed below.

The spectral line analysis of Model A (Fig. 5*a*) shows that this scenario can be ruled out as the main source of FIR radiation from Mrk 231 (Fig. 4*a*): the continuum model predicts low T_{rad} (between 20 and 34 K for the different lines) but the observed absorption in the 65 μm line, with lower level energy of 290 K, requires a much higher T_{ex}. Furthermore, the 119 and 84 μm lines are expected to be in emission ($W < 0$) as soon as T_{ex} becomes higher than 20 and 25 K (which, on the other hand, is not possible for radiative excitation). With such a low value of T_{ex}, $W_{65\mu m}$ is negligible even with our adopted screen $N(\mathrm{OH}) = 10^{18}$ cm^{-2}, a value that overestimates $W_{53\mu m}$ by more than a factor of 2.

The above problems still remain to some extent in model B, when R_{eq} is reduced to 400 pc (Fig. 5*b*). Here the dust radiation temperatures allow the lines to be seen in absorption up to $T_{ex} \approx 40$ K; however, $W_{65\mu m}$ is underestimated by more than a factor of 2 for the adopted $N(\mathrm{OH}) = 3 \times 10^{17}$ cm^{-2}, yet this column density still overestimates the absorption of the 53 μm line. Although model B cannot account for the 65 μm line strength, a region of similar size but lower N(OH) could contribute to the observed absorptions of the 119, 84, and 53 μm lines.

The single-component model that best accounts for the four observed OH lines is model C, with $R_{eq} = 200$ pc (Fig. 5*c*). The corresponding continuum model (Fig. 4*c*), with $T_d = 74$ K, also fits the overall FIR continuum emission rather well. Significantly, our models in § 3.3 show that the excitation temperatures required to reproduce the observed equivalent widths, 40–60 K, are those computed at the cloud surface if the OH is excited by the infrared emission from a blackbody at $T_d = 74$ K. Finally, the dust

C^+, but with an extreme luminosity-to-gas mass ratio that limits the [C II] luminosity per unit of luminous power in the continuum. Our derived luminosity to H_2 mass ratio of 500 $L_\odot/M_\odot$ is high; future studies will indicate whether it can be applied to other ULIRGs with similar [C II] deficits.

Given the high C^+ column densities (a few $\times 10^{19}$ cm^{-2}) required to account for the [C II] 158 μm line emission, the H_2 columns derived toward the extended component are unlikely to be associated with non-overlapping star-forming regions surrounded by optically thick envelopes. A single PDR is not expected to have $N(C^+)$ in excess of a few $\times 10^{17}$ cm^{-2}. A scenario with a crowded population of PDRs overlapping along the line of sight is therefore more plausible. If a typical *single* OB stellar cluster emits up to 10^{39} erg s^{-1}, the maximum value found by Scoville et al. (2001) in M51 and also the luminosity of W49, then the number of single clusters to produce the Mrk 231 starburst luminosity of 10^{12} $L_\odot$ is $\gtrsim 4 \times 10^6$. If these clusters are concentrated in a disk of radius 460 pc and thickness 25 pc (DS98), the mean distance between neighbor clusters is only $\lesssim 1.5$ pc (see also Keto et al. 1992). Merging of PDRs may be compatible with some area filling factor if, for example, some spiral structure is invoked within the disk.

In NGC 1068, Spinoglio et al. (2005) observed the OH 119 μm line in emission against the continuum. On the basis of a possible XDR chemistry, and given the corresponding mass, density, and temperature that characterize the nuclear region, Spinoglio et al. (2005) suggested that the OH 119 μm emission line could be formed in that region. This option also relied on the fact that relatively weak FIR emission is expected to arise from the circumnuclear disk of the Seyfert 2 galaxy, so that the OH 119 μm line can be excited through collisions and emit above the continuum in these dense and warm environments. The situation is different for Mrk 231 and Arp 220. In these ULIRGs, the extremely high luminosity arising from the nuclear region, together with the high concentrations of gas there, make the nuclear FIR emission component very bright. Any possible emission in the 119 μm line will be obscured by the strong absorption, which in these objects is ~30 times stronger than the emission feature in NGC 1068. In addition, the strong FIR radiation density pumps higher-lying OH and H_2O levels, thus producing absorptions in the higher-excitation lines. The OH and H_2O molecules are therefore potentially powerful tracers of circumnuclear regions around AGNs. Future *Herschel* observations of Mrk 231 and other sources will allow us to apply the models developed in this paper to these sources, refine them accordingly, and will certainly give new insights into the physical and chemical conditions of bright infrared galaxies.

E. G.-A. thanks the Harvard-Smithsonian Center for Astrophysics for its hospitality. The authors would like to thank M. Wolfire for helpful discussions. Research was supported in part by NASA grant NAG5-10659 and NASA grant NNX07AH49G. Basic research in infrared astronomy at the Naval Research Laboratory is supported by 6.1 base funding. This research has made use of NASA's Astrophysics Data System.

REFERENCES

Aalto, S., Spaans, M., Wiedner, M. C., & Hüttemeister, S. 2007, A&A, 464, 193

Armus, L., et al. 2007, ApJ, 656, 148

Baan, W. A., Salzer, J. J., & Lewinter, R. D. 1998, ApJ, 509, 633

Boksenberg, A., Carswell, R. F., Allen, D. A., Fosbury, R. A. E., Penston, M. V., & Sargent, W. L. W. 1977, MNRAS, 178, 451

Braito, V., et al. 2004, A&A, 420, 79

Bryant, P. M., & Scoville, N. Z. 1996, ApJ, 457, 678

Carilli, C. L., Wrobel, J. M., & Ulvestad, J. S. 1998, AJ, 116, 1007

Clegg, P. E., et al. 1996, A&A, 315, L38

Condon, J. J. 1992, ARA&A, 30, 575

Cutri, R. M., Rieke, G. H., & Lebofsky, M. J. 1984, ApJ, 287, 566

Davies, R. I., Tacconi, L. J., & Genzel, R. 2004, ApJ, 613, 781

Dickman, R. L. 1978, ApJS, 37, 407

Downes, D., & Eckart, A. 2007, A&A, 468, L57

Downes, D., & Solomon, P. M. 1998, ApJ, 507, 615 (DS98)

Draine, B. T. 1985, ApJS, 57, 587

Farrah, D., Afonso, J., Efstathiou, A., Rowan-Robinson, M., Fox, M., & Clements, D. 2003, MNRAS, 343, 585

Fischer, J., et al. 1999, Ap&SS, 266, 91

Gallagher, S. C., Brandt, W. N., Chartas, G., Garmire, G. P., & Sambruna, R. M. 2002, ApJ, 569, 655

González-Alfonso, E., & Cernicharo, J. 1997, A&A, 322, 938

———. 1999, ApJ, 525, 845

González-Alfonso, E., Smith, H. A., Fischer, J., & Cernicharo, J. 2004, ApJ, 613, 247 (Paper I)

Graciá-Carpio, J., García-Burillo, S., Planesas, P., & Colina, L. 2006, ApJ, 640, L135

Green, S., Maluendes, S., & McLean, A. D. 1993, ApJS, 85, 181

Harvey, V. I., et al. 1999, in The Universe as Seen by *ISO*, ed. P. Cox & M. F. Kessler (ESA-SP 427; Noordwijk: ESA), 889

Henkel, C., Guesten, R., & Baan, W. A. 1987, A&A, 185, 14

Kaufman, M. J., Wolfire, M. G., Hollenbach, D. J., & Luhman, M. L. 1999, ApJ, 527, 795

Kessler, M. F., et al. 1996, A&A, 315, L27

Keto, E., Ball, R., Arens, J., Jernigan, G., & Meixner, M. 1992, ApJ, 387, L17

Klöckner, H.-R., Baan, W. A., & Garrett, M. A. 2003, Nature, 421, 821

Kruegel, E., & Siebenmorgen, R. 1994, A&A, 288, 929

Lahuis, F., et al. 2007, ApJ, 659, 296

Launay, J.-M., & Roueff, E. 1977a, J. Phys. B, 10, 879

———. 1977b, A&A, 56, 289

Leitherer, C., et al. 1999, ApJS, 123, 3

Luhman, M. L., Satyapal, S., Fischer, J., Wolfire, M. G., Sturm, E., Dudley, C. C., Lutz, D., & Genzel, R. 2003, ApJ, 594, 758

Luhman, M. L., et al. 1998, ApJ, 504, L11

Malhotra, S., et al. 2001, ApJ, 561, 766

Meijerink, R., & Spaans, M. 2005, A&A, 436, 397

Meurer, G. R., Heckman, T. M., Lehnert, M. D., Leitherer, C., & Lowenthal, J. 1997, AJ, 114, 54

Offer, A. R., van Hemert, M. C., & van Dishoeck, E. F. 1994, J. Chem. Phys., 100, 362

Papadopoulos, P. P., Isaak, K. G., & van der Werf, P. P. 2007, ApJ, 668, 815 (PIW07)

Planesas, P., Scoville, N., & Myers, S. T. 1991, ApJ, 369, 364

Preibisch, Th., Ossenkopf, V., Yorke, H. W., & Henning, Th. 1993, A&A, 279, 577

Richards, A. M. S., Knapen, J. H., Yates, J. A., Cohen, R. J., Collett, J. L., Wright, M. M., Gray, M. D., & Field, D. 2005, MNRAS, 364, 353

Rieke, G. H. 1976, ApJ, 210, L5

Rigopoulou, D., Lawrence, A., & Rowan-Robinson, M. 1996, MNRAS, 278, 1049

Roche, P. F., & Chandler, C. J. 1993, MNRAS, 265, 486

Sanders, D. B., Mazzarella, J. M., Kim, D.-C., Surace, J. A., & Soifer, B. T. 2003, AJ, 126, 1607

Sanders, D. B., & Mirabel, I. F. 1996, ARA&A, 34, 749

Sembach, K. R., & Savage, B. D. 1996, ApJ, 457, 211

Scoville, N. Z. 2004, in ASP Conf. Ser. 320, The Neutral ISM in Starburst Galaxies, ed. S. Aalto, S. Hüttemeister, & A. Pedlar (San Francisco: ASP), 253

Scoville, N. Z., Polletta, M., Ewald, S., Stolovy, S. R., Thompson, R., & Rieke, M. 2001, AJ, 122, 3017

Skinner, C. J., Smith, H. A., Sturm, E., Barlow, M. J., Cohen, R. J., & Stacey, G. J. 1997, Nature, 386, 472

Smith, P. S., Schmidt, G. D., Allen, R. G., & Angel, J. R. P. 1995, ApJ, 444, 146

Soifer, B. T., et al. 2000, AJ, 119, 509

Spinoglio, L., Malkan, M. A., Smith, H. A., González-Alfonso, E., & Fischer, J. 2005, ApJ, 623, 123

Sturm, E., et al. 1998, in ASP Conf. Ser. 145, Astronomical Data Analysis Software and Systems VII, ed. R. Albrecht, R. N. Hook, & H. A. Bushouse (San Francisco: ASP), 161

Swinyard, B. M., et al. 1996, A&A, 315, L43

Tacconi, L. J., Genzel, R., Lutz, D., Rigopoulou, D., Baker, A. J., Iserlohe, C., & Tecza, M. 2002, ApJ, 580, 73
Takano, S., Nakanishi, K., Nakai, N., & Takano, T. 2005, PASJ, 57, L29
Taylor, G. B., Silver, C. S., Ulvestad, J. S., & Carilli, C. L. 1999, ApJ, 519, 185
Ulvestad, J. S., Wrobel, J. M., & Carilli, C. L. 1999, ApJ, 516, 127
Vastel, C., Polehampton, E. T., Baluteau, J.-P., Swinyard, B. M., Caux, E., & Cox, P. 2002, ApJ, 581, 315
Wolfire, M. G., Tielens, A. G. G. M., & Hollenbach, D. 1990, ApJ, 358, 116
Wright, C. M., van Dishoeck, E. F., Black, J. H., Feuchtgruber, H., Cernicharo, J., González-Alfonso, E., & de Graauw, Th. 2000, A&A, 358, 689
Yang, M., & Phillips, T. 2007, ApJ, 662, 284